Radiometric Estimation of Tropospheric Attenuation: A Mixed Physically Based/Machine Learning Approach

Tuna Tunçkol, Marianna Biscarini, *Senior Member, IEEE*, and Lorenzo Luini, *Senior Member, IEEE*

***Abstract*— A mixed physically based/machine learning (ML) approach to measure tropospheric attenuation A in all-weather conditions by means of microwave radiometers (MWRs) is proposed. The key idea is to combine the advantages originating from the accurate radiometric A retrievals, provided by the well-established Cosmic background (CB) approach in clear-sky conditions, with the benefits coming from ML techniques. The latter aim at estimating A in rainy situations through a simplified approach able to overcome the issues posed by more complex techniques such as the standard solution of the radiative transfer equation or the Sun tracking (ST) microwave technique. To this aim, an artificial neural network (ANN) is devised to turn the antenna noise temperatures measured by a four-channel MWR (from Ka- to W-band) into tropospheric attenuation at the frequencies of the radiometric channels, namely 23.8, 31.4, 72.5, and 82.5 GHz. The network is properly trained and tested by taking advantage of the concurrent CB and ST measurements collected by the RpG radiometer deployed at Politecnico di Milano, Milan, Italy, under the ESA-funded WRAD project. The proposed approach to retrieve the tropospheric attenuation is intended to overcome the limits associated both with the ST technique (only measurements during the day, link elevation strictly bound to the Sun ecliptic) and to the CB one (unreliable measurements in rainy conditions).**

***Index Terms*— Artificial neural network (ANN), atmospheric attenuation, mean radiating temperature, radiometry, rain attenuation, satellite communications.**

I. Introduction

SINCE the launch of the first communication-oriented commercial satellite in 1964 (Syncom 3), Earth-space communication systems have been characterized by a continuous increase in the carrier frequency, induced by the request for faster data rate (which implies wider bandwidths), by the technology advancement of microwave components and by the congestion of lower bands. The employment of Q/V-bands in high throughput satellites (HTS) systems is rapidly taking place, and the utilization of the W-band (75–110 GHz) emerges as the following step [1]. However, the higher the carrier frequency, the more detrimental the influence of the troposphere on electromagnetic waves: wave phase delay, signal group delay, wave depolarization, signal attenuation (as a result of absorption and scattering), ray bending, signal scintillation, and atmospheric noise contribution are some of the effects that cause the degradation of the link quality and the decrease in the link availability. Among them, attenuation certainly plays the most relevant role [2].

Designing Earth-space communication links at W-band currently represents a challenge. On the one side, the availability of W-band propagation data is limited to terrestrial links, with the sole exception of the LEO-based experimental activity carried out in the framework of the ESA project "CubeSat-based W-band Channel Measurements" [3]. On the other side, the existing propagation models (e.g., those included in [4]) were mostly developed and tested based on the data gathered from experimental activities at frequencies up to the V-band: the maximum frequency of the measurements collected from geostationary Earth orbit (GEO) satellites is 49.5 GHz (Italsat experiment). As a matter of fact, the accuracy of propagation models for the system design at the W-band remains an open question, which cannot be currently answered: there is a clear need for propagation measurements beyond 50 GHz.

This goal can be achieved through different kinds of experimental campaigns. The utilization of space-borne beacon signals offers an optimum option: the Alphasat Aldo Paraboni Experiment is the most recent (and currently ongoing) example of how long-term (Ka-band and Q-band) propagation data can be concurrently collected in several sites [5]. However, besides the current lack of W-band payloads onboard geostationary satellites (ideal orbit to guarantee measurement continuity), these kinds of experiments are complex and extremely expensive. In general, space-borne signals, also those emitted by commercial satellites at the Ku-band and Ka-band, can be used to collect data on the precipitation along the link [6], which can be in turn used to derive attenuation at higher frequencies.

A simpler and cheaper alternative is offered by ground-based microwave radiometers (MWRs), which

Manuscript received 15 May 2023; revised 14 September 2023, 14 November 2023, and 29 February 2024; accepted 18 April 2024. Date of publication 25 April 2024; date of current version 6 May 2024. This work was supported in part by the European Space Agency (ESA) through "WRAD—Characterization of W-Band Propagation Channel Through Ground-Based Observations (Expro Plus)" under ESTEC Contract 4000125141/18/NL/AF and in part by the European Office of Aerospace Research and Development (EOARD) through "MMWAP–MilliMeter Wave Atmospheric Propagation: Advancing Microphysical-Radiative Modeling, Statistical Characterization and Neural-Network Prediction of Cloud Attenuation and Emission" under Award FA8655-22-1-7171. *(Corresponding author: Lorenzo Luini.)*

Tuna Tunçkol is with Fergani Space Technologies, 34330 Istanbul, Turkey (e-mail: tuna.tunckol@mail.polimi.it).

Marianna Biscarini is with the Department of Information Engineering, Electronics and Telecommunications (DIET), Sapienza University of Rome, 00184 Rome, Italy (e-mail: marianna.biscarini@uniroma1.it).

Lorenzo Luini is with the Dipartimento di Elettronica, Informazione e Bioingegneria, Politecnico di Milano, 20133 Milan, Italy (e-mail: lorenzo.luini@polimi.it).

Digital Object Identifier 10.1109/TGRS.2024.3393506

can be employed to characterize the tropospheric channel by taking advantage of retrieval algorithms receiving as input the measured sky noise data. The most common MWR operation mode consists of pointing the instrument at the zenith or toward a satellite to collect brightness temperature data, which are converted into tropospheric attenuation by means of a simple inversion algorithm. This technique, referred to as "Cosmic background" (CB) operation mode for convenience of this article, typically offers accurate results [7], [8], but its applicability is limited to cases when scattering can be neglected: in rainy conditions, radiometric retrievals of the tropospheric attenuation can significantly deviate from the reference beacon-derived data [9]. Indeed, at Ka-band and above, although there is still a significant impact of absorption and emission under rainy conditions, scattering effects must be considered too [10], [11]. A recently developed more complex technique, commonly referred to as "Sun tracking" (ST) operation, consists of alternatively switching the MWR antenna azimuth angle from toward the Sun to off the Sun (for a fixed elevation angle) while gradually changing the elevation angle to track the diurnal Sun trajectory [12], [13]. The utilization of the Sun as a sort of equivalent beacon emitter offers the possibility to retrieve the tropospheric attenuation in all weather conditions, including rainy ones. Unfortunately, accurate ST measurements can present a challenge: pointing precisely at the Sun, which can be assimilated to a transmitter circular antenna whose half-power beamwidth is approximately 0.5°, might not be an easy task. This is even more challenging at the W-band, due to the reduction in the antenna beamwidth [14]. In addition, ST measurements are obviously available only during the day.

This contribution proposes a novel machine learning (ML) based approach to collect data on tropospheric attenuation A in all-weather conditions by exploiting MWRs. ML and neural network techniques are in rapid expansion in basically every scientific area. In the remote sensing field, the first approaches were developed for image processing, classification, prediction, and geophysical retrieval in general, with an increase in the last decades of techniques for the estimation of rainfall exploiting satellite passive observations [15], [16], [17]. In [18], an attempt to design a model-based neural network approach for the estimation of the atmospheric extinction exploiting ground-based observations is proposed, where radiometric observations are completed with a specific rainfall radiative model in order to overcome the limitations of classical radiometric observations in rainy conditions. Wu et al. [19] propose an ML technique for the brightness temperature estimation with the limitation of assuming a constant value of the mean radiating temperature (which is the core quantity for the retrieval of the atmospheric attenuation through ground-based microwave radiometric measurements). To the authors' knowledge, currently, there are no works devoted to the retrieval of the atmospheric mean radiating temperature through an ML approach, which is what is proposed in this work. Specifically, in this article, an artificial neural network (ANN) is devised and used to convert the brightness temperatures measured by a four-channel MWR into tropospheric attenuation at the frequencies of the radiometric channels, namely 23.8, 31.4, 72.5, and 82.5 GHz. The network is properly trained and tested by taking advantage of the concurrent CB and ST measurements collected by the RpG radiometer deployed at Politecnico di Milano, Milan, Italy, in the framework of the ESA-funded project "WRAD—Characterization of W-Band Propagation Channel Through Ground-Based Observations" [20]. This approach is intended to overcome the limits associated both with the ST technique (only measurements during the day, link elevation strictly bound to the Sun ecliptic) and the CB one (unreliable measurements in rainy conditions).

This contribution is organized as follows. Section II recalls the main concepts underpinning the estimation of the tropospheric attenuation from radiometric measurements, while Section III illustrates the experimental setup and the propagation data. Section IV focuses on the ML-based prediction technique, whose results and accuracy are discussed in Section V. Finally, Section VI presents some conclusions and offers some cues for future work.

II. MWR-Based Retrieval of the Tropospheric Attenuation

MWRs are passive instruments measuring the natural electromagnetic emission from tropospheric constituents, from which the associated attenuation can be retrieved by exploiting the radiative transfer equation (RTE) mathematical framework [21].

This goal can be mainly achieved by means of two measurement techniques briefly recalled in this section: the CB technique and the ST technique.

A. CB Technique

The interaction of electromagnetic radiation with atmospheric constituents is duly mathematically described by the RTE, which takes into account the electromagnetic absorption, emission, and scattering properties of the atmosphere. The Rayleigh-Jeans approximation of Planck's law, suitable for microwave frequencies, states that the electromagnetic emission of a blackbody, typically quantified in terms of brightness, is linearly dependent on its physical temperature. Thus, according to the RTE and adopting the Rayleigh-Jeans approximation, the overall sky thermal emission of a real body is referred to as brightness temperature T_B. If the considered real body is the Earth's atmosphere (i.e., the atmospheric constituents), the atmospheric brightness temperature for ground observation, that means considering the downwelling atmospheric radiation, is given by [21]

$$T_B(r) = T_B(0)e^{-\tau(0,r)} + \int_0^r k_e(r')\left[(1-a)T(r') + aT_{\mathrm{SC}}(r')\right]e^{-\tau(r',r)}\mathrm{d}r' \ (\mathrm{K}) \quad (1)$$

where $\vec{r} = r\vec{s}_0$ denotes the propagation direction within the Earth atmosphere, being $\vec{s}_0$ the unit vector indicating the observation direction. In (1), $T_B(r)$ is the brightness temperature observed at the point r (where we assume that the

ground receiving antenna is positioned), which consists of the contribution of an atmospheric layer starting at level 0 (that, in our case, is the top of the atmosphere): $T(r')$ is the physical temperature at the generic intermediate point r', $T_B(0)$ is the brightness temperature at the boundary layer (i.e., the CB temperature impinging on the top of the atmosphere $T_C = 2.73$ K), k_s is the scattering coefficient, k_e is the extinction coefficient, $a = k_s/k_e$ is the scattering albedo, τ is the optical thickness, and, finally, and $T_{\mathrm{SC}}(r)$ is the multiple scattering contribution. The latter is given by the radiation temperature coming from all the directions different from the considered propagation direction (i.e., scattered from the surrounding atmospheric particles), incident on the atmospheric particles located along the considered propagation direction, and scattered toward the observation direction.

Equation (1) can be written in a simplified form introducing the sky mean radiating temperature T_{mr} (defined as the temperature of the equivalent homogeneous isothermal atmospheric layer)

$$T_B(\theta, \varphi) = T_C e^{-\tau(\theta,\varphi)} + T_{\mathrm{mr}}\left[1 - e^{-\tau(\theta,\varphi)}\right] \text{ (K)} \tag{2}$$

where the propagation direction is expressed through the antenna azimuth φ and elevation θ angles.

Recalling that the atmospheric attenuation is $A(\theta, \varphi) = -10\log_{10}[e^{-\tau(\theta,\varphi)}]$ and by defining the antenna noise temperature T_A as the convolution between brightness temperature impinging on the antenna and the antenna directivity $D(\theta, \varphi)$

$$T_A(\theta, \varphi) = \frac{1}{4\pi}\int_{4\pi} T_B(\theta, \varphi) D(\theta, \varphi) d\Omega \text{ (K)} \tag{3}$$

it follows that:

$$A(\theta, \varphi) = 10\log_{10}\left(\frac{T_{\mathrm{mr}} - T_C}{T_{\mathrm{mr}} - T_A(\theta, \varphi)}\right) \text{ (dB)}. \tag{4}$$

As a result, (4) allows retrieving A, the attenuation along the path in dB, from the measured antenna noise temperature and the CB temperature (hence, the technique name), provided that an estimate of T_{mr} is available. In scattering-free conditions, T_{mr} can be quite accurately estimated from surface meteorological data [22], while in rainy ones, i.e., when k_s in (1) cannot be neglected, usual estimates of T_{mr} are not sufficiently accurate [23]: indeed, this is the main weakness to the use of the CB technique. Such limitation can be overcome when a radiometer and a beacon receiver are pointed along the same path, which allows deriving an accurate estimate of T_{mr} as illustrated e.g., in [24] and [25]. In the absence of a beacon receiver, different methodologies have been investigated in the past to estimate T_{mr} under scattering-free conditions from surface meteorological data. In this work, we take advantage of the model described in the Appendix: T_{mr} is estimated from the surface temperature T_S (K) and the surface relative humidity RH_S (%), while taking in due account the dependence of T_{mr} on the elevation angle [8].

The main issue for the CB methodology is that, using T_{mr} as obtained from (12) under rainy conditions, $T_A(\theta, \varphi)$ is likely to exceed T_{mr}, which makes unusable the outputs of (4) [12].

B. ST Technique

The idea underpinning the ST technique is to exploit the Sun as an equivalent space-borne electromagnetic radiator. In this case, two consecutive measurements are carried out by fixing the elevation angle θ_0 while switching the azimuth angle from φ_0 to φ_1 to alternatively point the instrument toward-the-Sun (twS) and off-the-Sun (ooS), respectively. In the former case, the brightness temperature measured by the MWR consists of the contribution coming from the Sun, attenuated by the atmosphere, as well as by the contribution of the atmospheric emission itself. In the latter case, the measurement is not affected by the Sun radiation, but only by atmospheric emission [12], [13].

The comprehensive mathematical framework of the ST technique is described in [12] and [13], in which the reader can find additional details; here, it suffices to focus on the key concepts. As previously stated, the ST technique foresees to alternatively switch the MWR antenna pointing from toward the Sun to off the Sun at a given elevation angle. This is continuously repeated as the elevation angle changes to track the Sun's diurnal trajectory. Using this approach, the tropospheric attenuation A_{ST} can be estimated as [12], [13]

$$A_{\mathrm{ST}}(\theta_0, \varphi_0) \cong 4.343 \ln\left[\frac{T^*_{B\mathrm{sun}}(\theta_0, \varphi_0)}{\Delta T_A(\theta_0, \varphi_0)}\right] \text{ (dB)} \tag{5}$$

where

$$\Delta T_A(\theta_0, \varphi_0) = T_{A-\mathrm{twS}}(\theta_0, \varphi_0) - T_{A-\mathrm{ooS}}(\theta_0, \varphi_1) \text{ (K)}. \tag{6}$$

$T_{A-\mathrm{twS}}(\theta_0, \varphi_0)$ and $T_{A-\mathrm{ooS}}(\theta_0, \varphi_1)$ are the antenna noise temperatures measured when pointing toward and off the Sun, respectively. $T^*_{B\mathrm{sun}}(\theta_0, \varphi_0)$ is the Sun brightness temperature multiplied by the beam-filling factor (f_Ω), i.e., the ratio between the Sun radiation solid angle ($\Omega_{P\mathrm{sun}}$) and the antenna beamwidth radiation solid angle ($\Omega_{P\mathrm{ant}}$), $f_\Omega = \Omega_{P\mathrm{sun}}/\Omega_{P\mathrm{ant}}$. The latter can be affected by how precisely the antenna can track the Sun [12], [13], [14]. For A_{ST} to be an accurate estimate of the tropospheric attenuation, changing between ooS and twS observations needs to be fast enough to assume the atmospheric homogeneity (i.e., same optical thickness and mean radiative temperature between two consecutive observations). This implies choosing φ_1 large enough to prevent the Sun from intersecting the field of view of the radiometer antenna. Note that (5) requires to first evaluate the Sun brightness temperature, to be performed in clear sky conditions, as detailed in [12].

The ST technique permits circumventing the issue of estimating T_{mr} by providing an attenuation retrieval method that is reliable in all weather conditions, though also such a technique presents some limitations. In fact, under severe rainy conditions, the contribution of the Sun becomes negligible due to the strong attenuation by rain particles. In this case, ΔT_A in (6) may reach zero or even negative values, depending on the radiometer noise and the atmospheric variability between φ_0 and φ_1. This poses an upper limit to the application of the ST technique for the retrieval of tropospheric attenuation under rainy conditions [12].

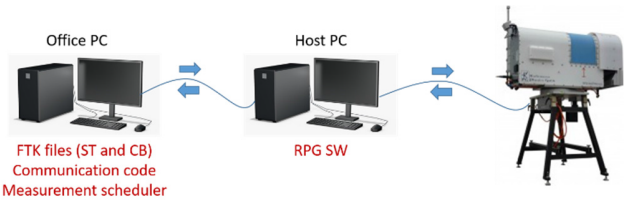

Fig. 1. Setup for automated radiometric measurements.

TABLE I
AVAILABILITY FOR THE MILANO ST MWR MEASUREMENTS

Band	Availability period
W	01/11/2020 – 15/01/2021 (Period 1)
Ka	01/11/2020 – 08/08/2021 (Period 2)

III. EXPERIMENTAL SETUP AND DATA COLLECTION

The radiometric data were collected in the framework of the WRAD project funded by the European Space Agency, which kicked off in 2019 to perform a W-band ST measurements campaign [20] (45.48°N, 9.23°E). The ST-MWR, deployed at Politecnico di Milan, features two channels at 23.8 and 31.4 GHz (Ka-band) and two channels at 72.5 and 82.5 GHz (W-band). The instrument is equipped with a hydrophobic radome and a blower, both of which contribute to significantly reducing the possible accumulation of water on the radome surface, which, in turn, might contaminate the measurements. The device was built by RPG Physics GmbH and takes advantage of azimuth and elevation positioners (0.05° and 0.1° scan step, respectively) to enable different measurement modes, namely: ST, CB, and file tracking (FTK). The latter mode is conceived for a custom operation of the instrument: the user can specify in an FTK file the daily time series of the elevation and azimuth angles that the positioners will set. Fig. 1 shows the architecture for the automated operation of the instrument: the Office PC produces the daily FTK files, executes the measurements schedule, and communicates with the Host PC, which runs the RPG software (SW) to control the radiometer. The measured data are stored on the Host PC and can be easily retrieved by the Office PC for post-processing.

The WRAD dataset is nominally available from October 2019 to August 2021, but the accuracy of the antenna pointing system was optimized only at the end of October 2020. In addition, around mid-January 2021 the noise diode of the W-band channels failed, which further limited the collection of W-band data. Table I reports the actual period of Ka- and W-band data availability between 2019 and 2021; two partially overlapping periods are defined: "Period 1" (for the W-band channel availability) and "Period 2" (for the Ka-band channel availability). Though the availability of W-band data is limited to approximately 2.5 months, these measurements definitely represent a valuable dataset, given the overall scarcity of such kind of data worldwide.

A weather station is installed at approximately 20 m from the MWR to monitor the surface pressure P, the relative humidity RH, and temperature T. At the same distance, a disdrometer is installed to measure the rain rate RR.

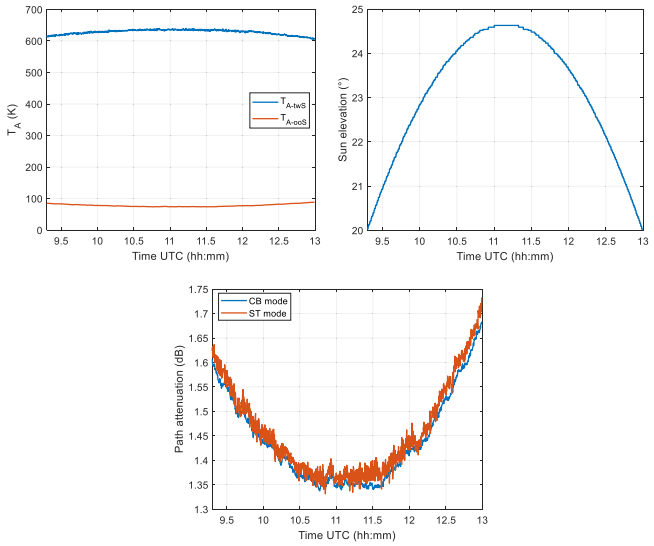

Fig. 2. Sample of the data measured by the ST-MWR during a clear sky day, at 72.5 GHz. From the top-left corner, in a clockwise direction: T_A, Sun elevation, and path attenuation.

Fig. 2 shows a sample of the data measured by the MWR during a clear sky day, at 72.5 GHz. The top left-hand corner graph depicts the trend of the equivalent noise temperature: $T_{A-\mathrm{ooS}}$ is maximum at low values of the Sun elevation (shown in the top right-end corner graph) because of the longer tropospheric path, i.e., an increased sky noise contribution. On the contrary, $T_{A-\mathrm{twS}}$ is maximum in correspondence of the Sun elevation peak because the Sun radiation is less attenuated by the atmosphere, if compared to low elevations. Fig. 2 also shows that the path attenuation estimated using the ST mode is in very good agreement with the one estimated using the CB mode (bottom graph), which is the reference for atmospheric attenuation in the absence of precipitations [7].

Further results are shown in Fig. 3, which reports the measurements collected during a rain event (see the bottom left-hand graph depicting RR): as expected, there is a marked discrepancy between the CB mode and ST mode attenuations, the latter being the reference method under rainy conditions (because of the impact of atmospheric particle scattering on the CB method) [12].

IV. NEURAL NETWORK-BASED APPROACH

The results in Fig. 3 show that the attenuation difference between the ST and the CB techniques reaches a peak of 3.5 dB, which gives a hint of how unreliable the latter approach can be under rainy conditions. On the other hand, accurate ST measurements are challenging: pointing precisely at the Sun might not be an easy task, even more so at the W-band, due to the reduction in the antenna beamwidth [14]. In addition, ST measurements cannot be collected at night time.

This section proposes a new approach aimed at estimating the tropospheric attenuation from radiometric measurements: the objective is to preserve the advantages offered by the ST technique (application in all weather conditions and high accuracy), while circumventing the associated challenges, i.e., precise Sun pointing and collection of the data only during the day. This goal can be achieved by resorting to an ANN,

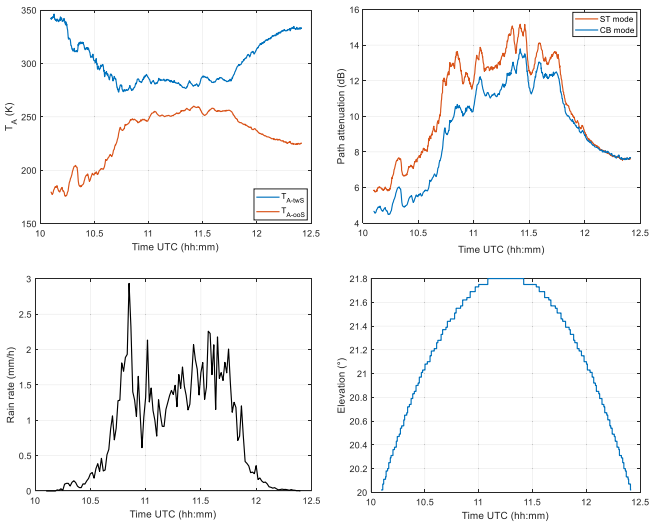

Fig. 3. Sample of the data measured by the ST-MWR during a rainy day, at 72.5 GHz. From the top-left corner, in the clockwise direction: T_A, path attenuation, rain rate, and Sun elevation.

receiving as input T_A measurements collected using the CB approach (as well as meteorological ones), and providing as output an estimate of the mean radiating temperature T_{mr}. From the knowledge of the latter, the tropospheric attenuation A can be calculated using (4). As described in detail in the subsections below, the network training will take advantage of the concurrent ST and CB measurements collected during the WRAD campaign.

A. Data Preparation

The power of ANNs lies in the fact that they provide a simple tool to model the relationship between given inputs and outputs, which is especially useful if such a relationship is mathematically complex and/or no closed-form solution exists. This is the case of the RTE in scattering conditions.

Fig. 4 depicts the inputs and outputs of the proposed ANN: the network is fed with the information provided by the weather sensors and with the off the Sun radiometric measurements, $T_{A-\mathrm{ooS}}$, which de facto correspond to CB measurements. Although the rain rate measured at one point is not fully representative of the precipitation along the whole (slant) path, it is still expected to be a paramount input parameter. The network output is the mean radiating temperature T_{mr}, which is a key parameter driving the prediction of the tropospheric attenuation through (4) [26]. It is worth pointing out that $T_{A-\mathrm{ooS}}$ in Fig. 4 includes all the available radiometric measurements, while T_{mr} is estimated for a specific frequency channel: though the network structure will not change, a different set of coefficients will be derived for each of the four frequencies. A further note is necessary on this point for the sake of clarity: as the data availability periods in Table I are different for the two bands, for Period 1, four channels were used as input to the network, while for Period 2, only the Ka-band ones were employed (as no W-band data are available in that period).

The target values of T_{mr}, necessary to train the ANN, are derived from the peculiar WRAD dataset. Specifically, (4) is

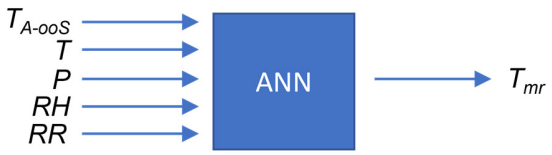

Fig. 4. Inputs and outputs of the proposed ANN.

inverted as follows:

$$T_{\mathrm{mr}} = \frac{kT_{A-\mathrm{ooS}}(\theta_0, \varphi_1) - T_C}{1-k} \ (\mathrm{K})$$
$$k = 10^{\frac{A_{\mathrm{ST}}(\theta_0,\varphi_0)}{10}}. \tag{7}$$

When training an ANN, it is often required to scale the input data to improve the network accuracy, especially if the range of variation of the input features is strongly different, which is the case for the ANN reported in Fig. 4. The most common scaling techniques are normalization and standardization [27], [28], the latter being considered in this work. Standardization consists of scaling the original input feature X into a new variable X_n whose mean value is 0 and whose standard deviation is 1

$$X_n = \frac{X-\mu}{\sigma} \tag{8}$$

where μ and σ are the mean and standard deviation values of X, respectively.

In addition, the logarithmic transformation is applied to the target data Y to obtain the new variable Y_n that has a more skewed distribution of the output, which, in turn, contributes to increasing the network accuracy [29]

$$Y_n = \log(Y). \tag{9}$$

Another key step in the design of an ANN is to divide the available dataset into different subsets, each one used for a different purpose: training, validation, and testing [30]. The first set of data is used to train the model, i.e., to derive the coefficients that map at best the inputs to the outputs. The test dataset contains samples that are not used for training, so they can be employed to assess independently the accuracy of the outputs provided by the network. Finally, the validation data are used to avoid overfitting, i.e., the network offers an extremely high accuracy only when using the training dataset, and consequently, a poor performance on any other additional data. It is common to initially isolate 10%–20% of total data for the test, the remaining part being employed for training. Afterward, a further split could be applied (25%) to training data to extract the validation dataset. In this work, approximately 10% of Ka-band data and 15% of W-band data are reserved for testing. The remaining data (90% and 85% for the Ka-band and W-band, respectively) then are split into 75% for training and 25% for validation. With the aim of maximizing the effectiveness of the ANNs, the available data were selected for training/validation or testing based on the rationale of maintaining the same balance between rainy days and clear-sky days in each of the datasets: in fact, the dynamics of the tropospheric attenuation under rainy conditions is expected to be much higher (i.e., the estimation more difficult) than during clear sky days. Specifically, Table II lists

TABLE II
CLEAR-SKY AND RAINY DAYS SELECTED TO TEST THE ANNS

Frequency (GHz)	Rain free days	Rainy days
23.84	4-28 Nov 2020 25 Jan 2021 21 Feb 2021 10 Mar 2021 5-17 Apr 2021 10-25 Jun 2021 10-19 Jul 2021 6 Aug 2021	9-20 Dec 2020 2-21 Jan 2021 3 Feb 2021
31.4	7-29 Nov 2020 16 Dec 2020 28 Jan 2021 1-14 Feb 2021 14-21 Mar 2021 18 May 2021 1-28 Jun 2021 8 Aug 2021	1-8-20 Dec 2020 4 Jan 2021 11 Apr 2021
72.5	5-24-29 Nov 2020 16 Dec 2020 8 Jan 2021	9-20-24 Dec 2020 2 Jan 2021
82.5	10-29 Nov 2020 17-31 Dec 2020 7 Jan 2021	8-20-24 Dec 2020 2 Jan 2021

the clear-sky and rainy days selected to test the ANNs, while the remaining ones were employed for the training/validation phase.

The identification of rainy days was achieved by relying both on the collocated weather sensors (mainly the rain rate) and on the visual inspection of the data. In fact, the disdrometer provides point measurements of the precipitation, which is not always representative of the signature of rain on the signal along the slant path.

B. Model Development

The ANN development was achieved by taking advantage of the MATLAB Deep Learning Toolbox. Specifically, the "fitrnet" function was used to train the network [31]. This function trains ANNs with the fully connected feed-forward multilayer perceptron (MLP) architecture, using the Limited Memory Braydon Fletcher Goldfarb Shannon (L-BFGS) optimization algorithm. The function optionally applies the input data standardization. The overall implementation of the network is summarized in Fig. 5.

A different network model is obtained for each frequency channel: the details of each network are summarized in Table III. The number of hidden layers and neurons is determined by following the straightforward "trial-and-error" approach: the network complexity was gradually increased until no further significant improvements in the accuracy were achieved, as further detailed in the next Section. Regarding the neuron activation function, the rectified linear unit (reLU) was chosen.

The selection of the number of hidden layers and neurons is typically the result of a compromise. On the one hand, a small number of hidden layers and neurons will yield limited accuracy, as the ANN will not be able to properly represent the complex relationship between the input and the output data. On the other hand, large network architectures could result in a high computational burden (and sometimes overfitting),

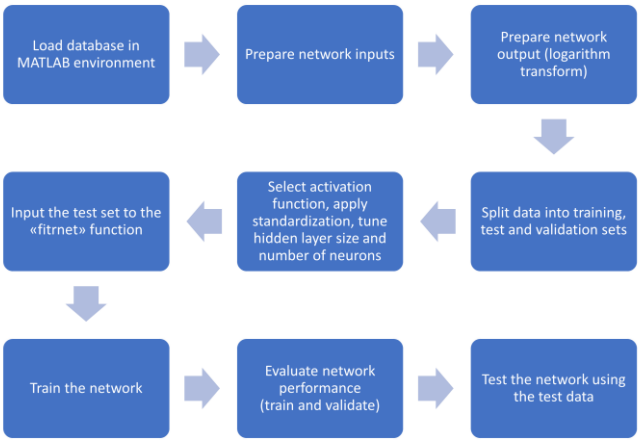

Fig. 5. Flowchart summary of the network training and test.

TABLE III
DETAILS ON THE ANNS

Frequency (GHz)	Number of hidden layers	Number of neurons
23.84	3	[11,8,5]
31.40	3	[11,8,5]
72.50	2	[12,7]
82.50	2	[15,6]

especially while working with large datasets. In this regard, the difference in the number of hidden layers indicated in Table III might depend on the type of events predicted at the different frequencies. W-band data are only available for late Autumn and early Winter (Period 1), both characterized only by stratiform events (slow variations in time and limited rain intensity). On the other hand, Ka-band data cover a longer period (Period 2) including different seasons, i.e., both stratiform and convective events (quick variation in time and high rain intensity). As the networks associated with Ka-band channels allow predicting T_{mr} under diversified rainy conditions (stratiform and convective), their complexity can be expected to be higher than the one associated with W-band networks.

The performance of the network can be quantified by inspecting the loss scores after each training, all expressed in terms of mean squared error (MSE). It is common practice to consider two types of loss scores: training and validation. The former is a more general indicator of the network accuracy: it is calculated on the testing dataset and it is used to iteratively update the network parameters (weights and biases). The latter is calculated on the validation dataset to point out possible overfitting: this occurs when the two loss scores diverge at some point in the training process. Fig. 6 offers a typical example of the convergence of the abovementioned losses for successful network training ($f = 31.40$ GHz).

The overall training results for each network are listed in Table IV.

V. RESULTS AND DISCUSSION

A. Daily Basis Analysis

The ANN performance can be assessed either by looking at the prediction of T_{mr}, or, more informatively, directly in terms

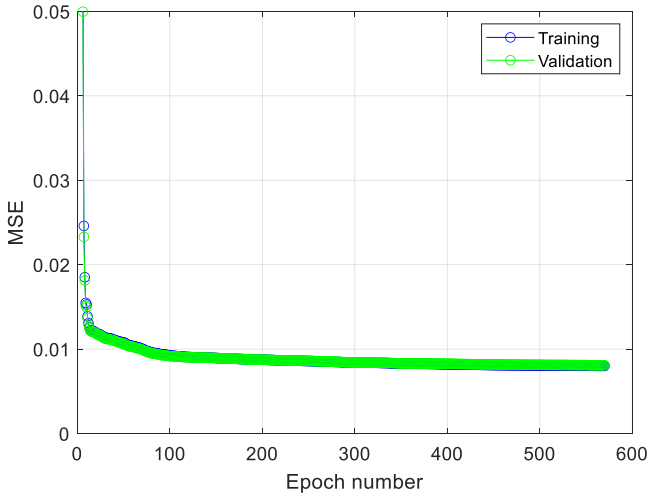

Fig. 6. Convergence of the training and validation losses for a successful network training ($f = 31.40$ GHz).

TABLE IV
TRAINING RESULTS FOR EACH NETWORK

Frequency (GHz)	MSE	Training time (s)
23.84 GHz	0.0076	10.7
31.40 GHz	0.0079	22.67
72.50 GHz	0.00041	0.675
82.50 GHz	0.00094	2.3

of the tropospheric attenuation A. Fig. 7 compares A for a clear-sky day (28 November 2020), as obtained by means of the ST (A_{ST}) and CB (A_{CB}) techniques (red solid line and yellow dashed line, respectively) and as estimated using the ANN (A_{NN}, blue solid line). In this case, all curves are in agreement: the CB technique is accurate in conditions with no scatter, the ST technique offers good accuracy in all weather conditions, and the ANN provides a precise prediction as well. A more critical comparison is offered for two rainy days in Fig. 8 (8 December 2020, light rain) and Fig. 9 (2 January 2021, moderate rain): as expected, the attenuation obtained from the ANN approach better agrees with the reference ST-based estimation, if compared to one derived from the application of the CB framework. The discrepancy increases with frequency due to the associated enhancement of the tropospheric effects moving from the Ka-band to the W-band. Fig. 9 clearly points out that the attenuation estimated through the CB approach reaches higher values as the precipitation intensity increases, thus leading to strong inaccuracies and, in most cases, to the overestimation of A (see Fig. 10): this is due to the inaccuracy of T_{mr} estimations obtained from surface parameters, under rain conditions.

A more complete assessment of the prediction accuracy can be obtained by evaluating the root mean square (rms) value of the absolute prediction error ε, defined as

$$\varepsilon(t) = A_{\mathrm{CB/ANN}}(t) - A_{\mathrm{ST}}(t) \ \mathrm{(dB)} \tag{10}$$

where $A_{\mathrm{CB/ANN}}(t)$ is the attenuation estimated using either the CB technique or the ANN approach, for every sample in a day, while $A_{\mathrm{ST}}(t)$ is the ST-based attenuation.

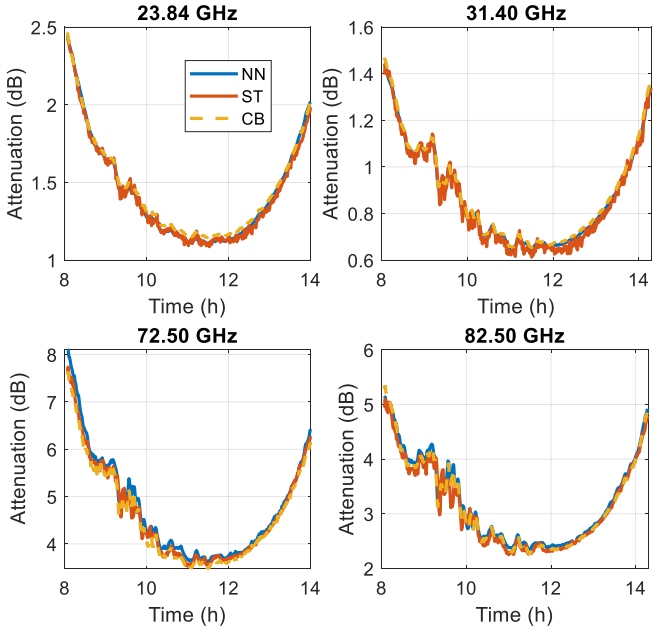

Fig. 7. Trend of the tropospheric attenuation on 28 November 2020 (clear sky), as estimated using the ST technique (red curve), the CB technique (yellow curve), and the neural network approach (blue curve).

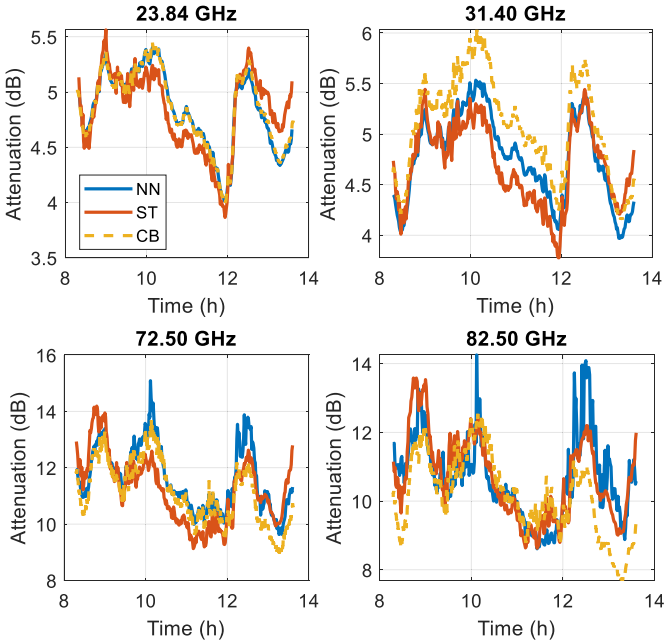

Fig. 8. Trend of the tropospheric attenuation on 8 December 2020 (light rain), as estimated using the ST technique (red curve), the CB technique (yellow curve), and the neural network approach (blue curve).

Figs. 11 and 12 depict the daily rms value, calculated by considering separately the rain-free days and the rainy ones, respectively. The former figure clearly indicates that the prediction performance of the two methods is quite high and fully comparable. In both cases, the rms value never exceeds 0.8 dB both at the Ka-band and W-band, respectively. The peak error in Fig. 11 at the Ka-band (≈0.5 dB at 23.84 GHz and ≈0.7 dB at 31.40 GHz) is associated with the overestimation of the attenuation using the ST method at the beginning of the day (elevation angle around 10°), in turn,

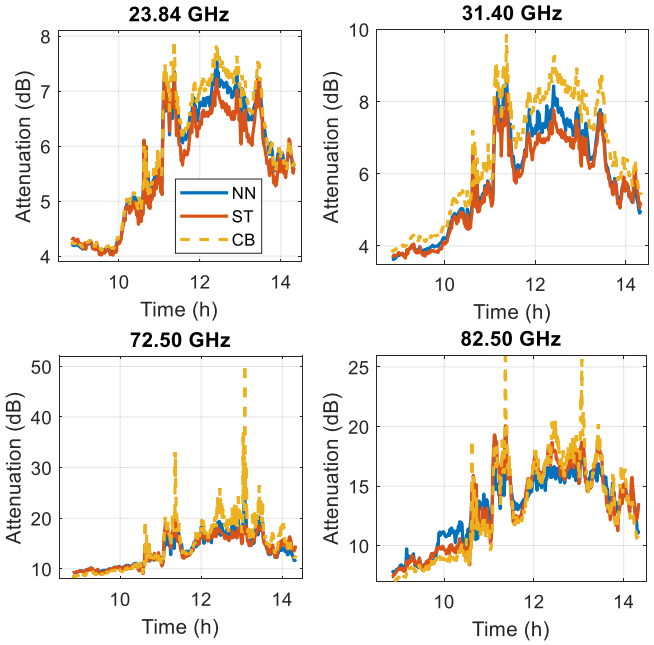

Fig. 9. Trend of the tropospheric attenuation on 2 January 2021 (moderate rain), as estimated using the ST technique (red curve), the CB technique (yellow curve), and the neural network approach (blue curve).

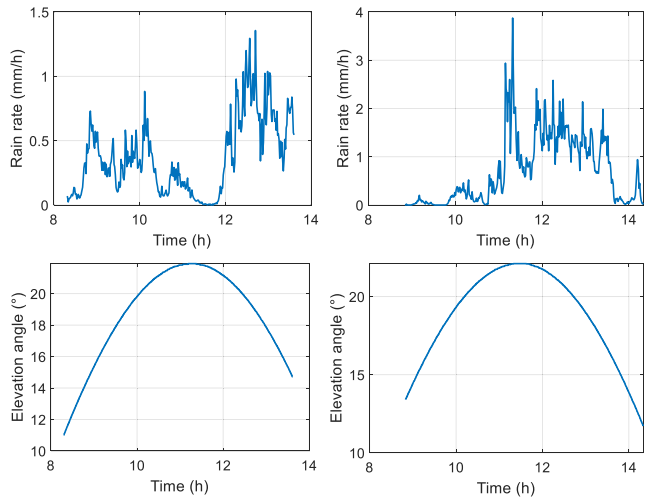

Fig. 10. Rain intensity trend and Sun elevation angles for 8 December 2020 (left side) and 2 January 2021 (right side).

likely due to an obstacle partially obstructing the path to the Sun (e.g., construction crane). As for rainy days, the results shown in Fig. 12 corroborate the findings reported in Figs. 8 and 9: while the rms associated with the ANN approach falls approximately below 2 and 2.5 dB at the Ka-band and W-band, respectively, the one obtained from the CB technique reaches peaks of roughly 4.5 and 5 dB at the Ka-band and W-band, respectively.

For the sake of completeness, Fig. 13 shows the same information as in Figs. 11 and 12, but considering only the ANN test dataset (rain-free plus rainy days).

B. Statistical Analysis

The statistical analysis of results is of key importance for system design purposes, more specifically to determine the atmospheric margin to be assigned to any Earth-space link.

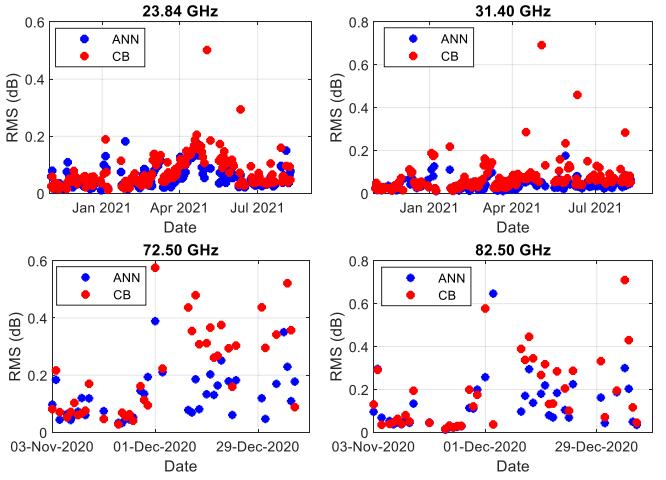

Fig. 11. RMS of the prediction error using the ANN approach (blue dots) and the CB technique (red dots): rain-free days (test plus training/validation datasets).

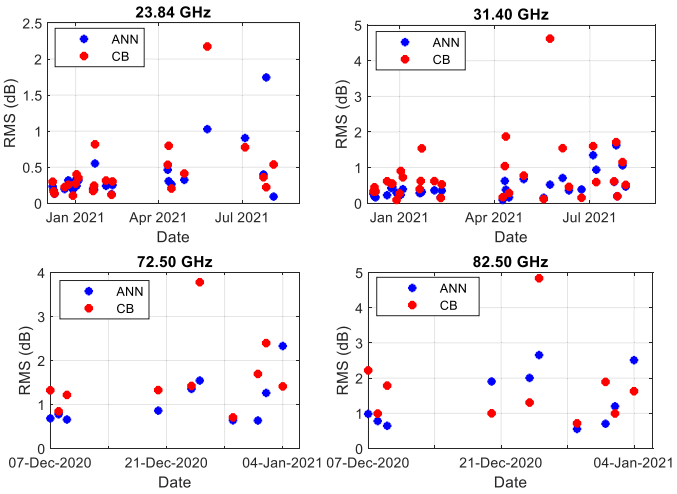

Fig. 12. RMS of the prediction error using the ANN approach (blue dots) and the CB technique (red dots): rainy days (test plus training/validation datasets).

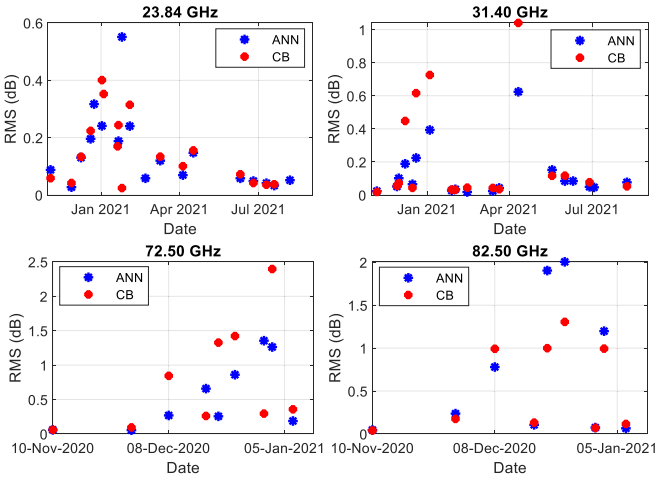

Fig. 13. RMS of the prediction error using the ANN approach (blue dots) and the CB technique (red dots): rain-free plus rainy days (only test dataset).

Figs. 14 and 15 depict the complementary cumulative distribution functions (CCDFs) of the A_{ST}, A_{CB}, and A_{NN}, at 31.40 and 82.50 GHz, respectively, for all the rain-free samples. As already pointed out in Section V-A, a very

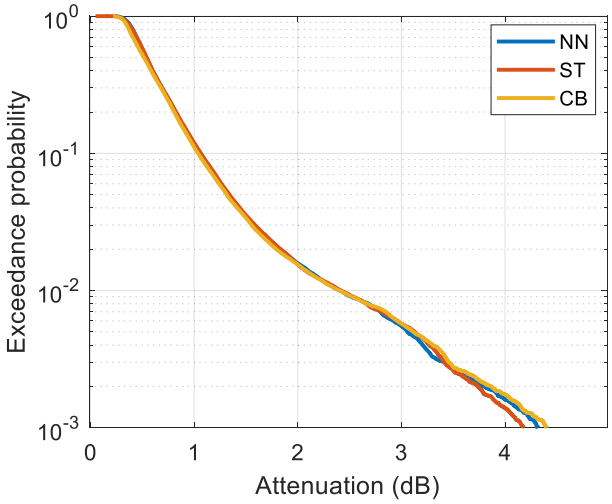

Fig. 14. CCDF of the tropospheric attenuation at 31.40 GHz under rain-free conditions.

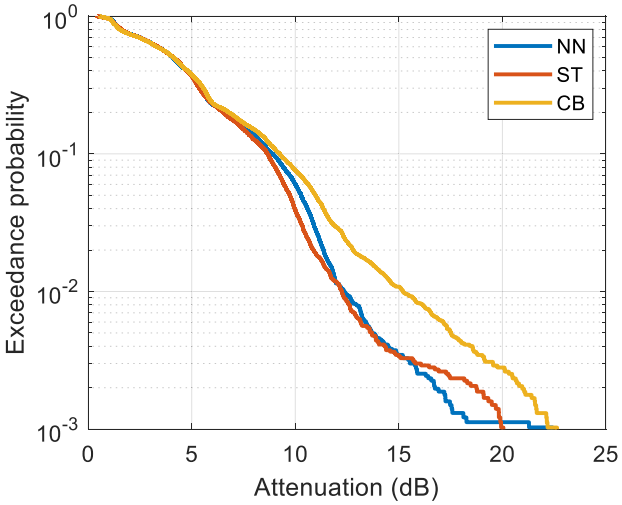

Fig. 16. CCDF of the tropospheric attenuation at 23.84 GHz under rainy conditions.

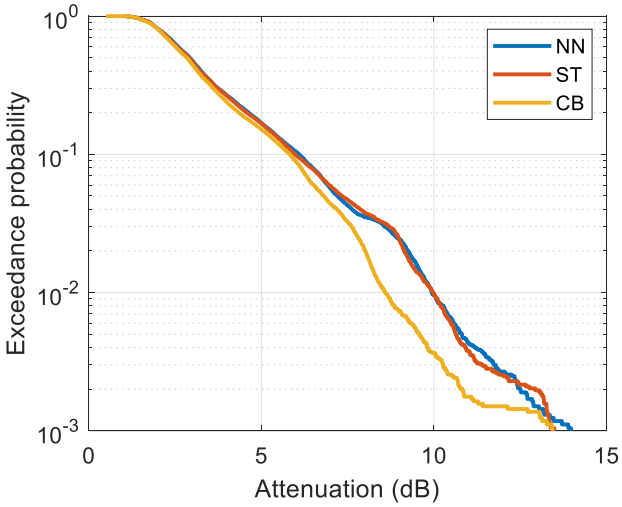

Fig. 15. CCDF of the tropospheric attenuation at 82.50 GHz under rain-free conditions.

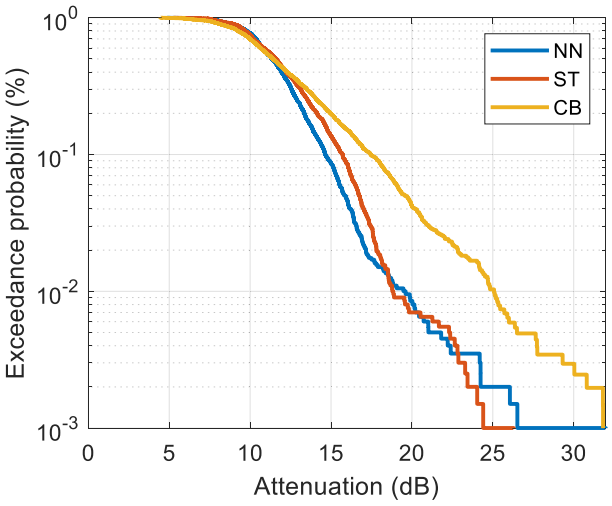

Fig. 17. CCDF of the tropospheric attenuation at 72.50 GHz under rainy conditions.

good agreement emerges at 31.40 GHz by comparing the different curves, while a slightly higher discrepancy is visible at 82.50 GHz, up to 1 dB for the exceedance probability P ranging roughly from 0.005 to 0.05.

As expected, a much larger difference between the different approaches appears in Figs. 16 and 17, which show the CCDFs of the tropospheric attenuation at 23.84 and 72.50 GHz, respectively, for all the rainy samples: the lower the probability value and the higher the frequency, the more marked is the overestimation of A_{CB} over A_{ST}, reaching approximately 15 dB for $P = 0.001$ and $f = 72.5$ GHz. On the contrary, the discrepancy between A_{NN} and A_{ST} is quite limited at both frequencies, thus indicating the ability of the neural network to provide accurate predictions of the tropospheric attenuation also under rainy conditions.

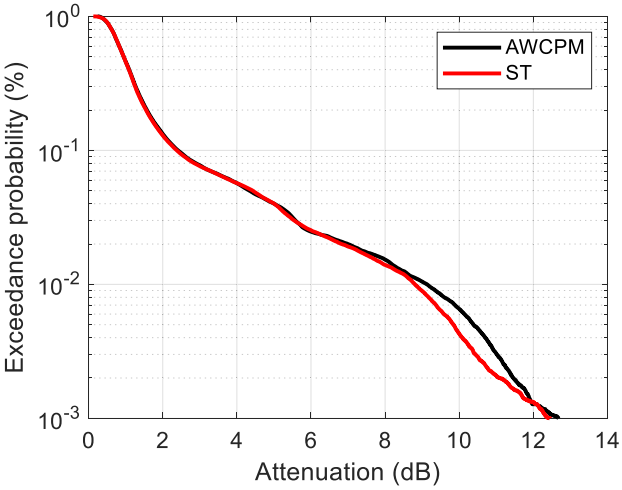

Fig. 18. CCDF of the tropospheric attenuation at 23.84 GHz: comparison between the application of the AWCPM and the ST technique.

C. All-Weather Combined Prediction Model

As discussed in Section II-A, the CB approach is a well-established technique allowing an accurate retrieval of the tropospheric attenuation in rain-free situations [7]. Moreover, whenever physically based closed-form inversions are available, they should be preferred over empirical or machine-learning techniques, which obviously have a lower

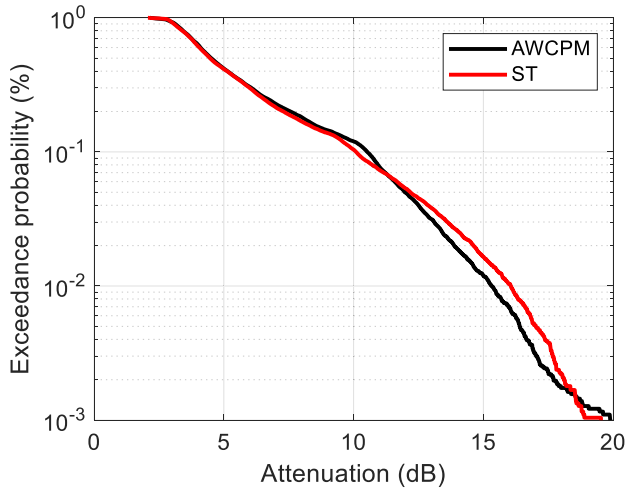

Fig. 19. CCDF of the tropospheric attenuation at 72.50 GHz: comparison between the application of the AWCPM and the ST technique.

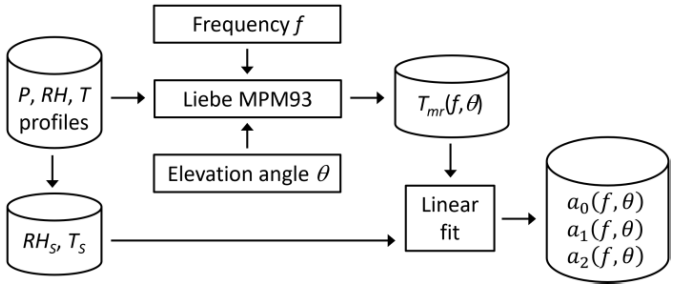

Fig. 20. Summary of the T_{mr} analytical model development process.

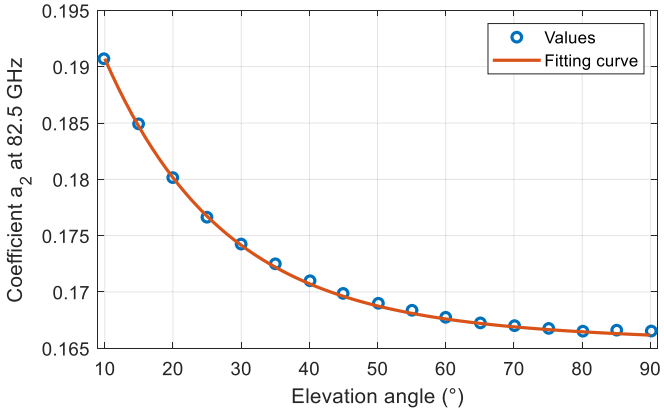

Fig. 21. Trend of coefficient a_2 in (12) at 82.5 GHz as a function of the elevation angle.

degree of global applicability. In this context, this section outlines a methodology to combine the advantages originating from the high accuracy of CB inversions in scattering-free conditions with those coming from the proposed ANN under rainy conditions. The key prerequisite is the ability to spot the presence of precipitation along the path, which can be achieved by resorting to the Sky Status Indicator (SSI), defined as [32]

$$\mathrm{SSI} = \frac{T_{A-\mathrm{ooS}}(31.40) - 9.19}{T_{A-\mathrm{ooS}}(23.84)}. \tag{11}$$

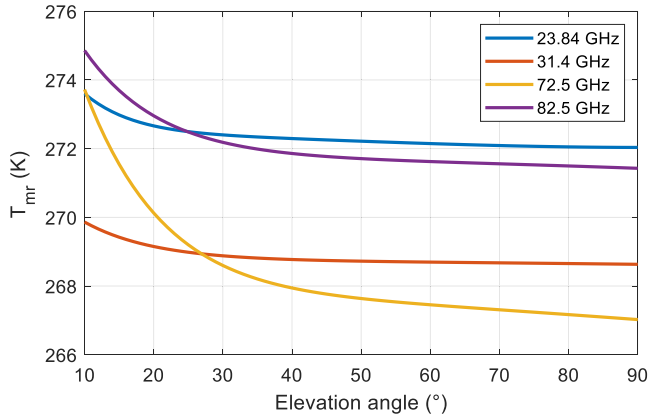

Fig. 22. Trend of T_{mr} as a function of the elevation angle according to the model in (12), for $T_S = 288$ K and $\mathrm{RH}_S = 50\%$.

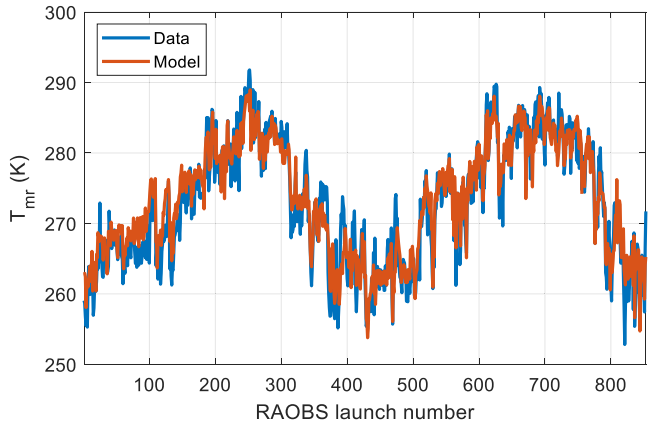

Fig. 23. Mean radiating temperature as calculated from the RAOBS profiles (see Fig. 20) and as estimated using the analytical model in (12); two full years of the available dataset, $f = 82.5$ GHz and $\theta = 45°$.

Setting different thresholds on the SSI allows having an estimate of the meteorological status along the path, namely as follows.

1) SSI < 0.4: clear sky;
2) $0.4 \leq$ SSI < 0.87: cloudy conditions;
3) SSI ≥ 0.87: rainy sky conditions.

Therefore, taking advantage of the SSI, the following All-Weather Combined Prediction Model (AWCPM) is devised.

1) For each instant, calculate the SSI from $T_{A-\mathrm{ooS}}$ at 23.84 and 31.40 GHz.
2) If SSI < 0.87 (scattering-free conditions), apply (4) to obtain A.
3) If SSI ≥ 0.87 (scattering conditions), apply the proposed ANN to derive A.

It is worth mentioning that the SSI is a statistical tool: 0.87 is a sort of average threshold maximizing the accuracy in identifying the presence of precipitation along the path [32]. The misidentification of meteorological conditions will typically occur for the heavy cloud/light rain cases, neither of which is critical for the retrieval method's accuracy. In fact, when SSI ≥ 0.87 but no rain is actually present along the path, the ANN has proven to be accurate. On the other hand, if SSI < 0.87, but some light rain is actually present, the CB

approach is still expected to provide accurate results, as the amount of scattering is quite limited. This is proven by the results reported in Figs. 18 and 19 at 23.84 and 72.50 GHz, respectively: the agreement between the retrievals obtained using the AWCPM and the ST technique, used as a reference, is very good for all exceedance probability values. Comparable results, not included for the sake of brevity, are obtained at 31.40 and 82.50 GHz.

VI. Conclusion

This work proposed a novel mixed physically-based/ML approach to measure tropospheric attenuation A affecting Earth-space links in all weather conditions. The measurement technique relies on the use of MWRs, and, as such, it offers a valid less expensive alternative to carrying out typical propagation experiments that exploit space-borne beacon signals. This is even more so at the W-band, for which no long-term measurements nor space-borne signals (from GEO satellites) currently exist. Moreover, the proposed approach combines the advantages originating from the accurate A retrievals provided by the well-established CB approach in clear-sky conditions with the benefits coming from ML techniques, which can offer a simplified solution for the estimation of A in rainy conditions, if compared to the application of the RTE and/or the ST technique.

Four ANNs were devised to convert the antenna noise temperature T_A measured by a four-channel Ka-band/W-band MWR into mean radiating temperature T_{mr} at 23.8, 31.4, 72.5, and 82.5 GHz, from which A can be easily derived. The networks, which also receive as input the local meteorological parameters, were properly trained and tested by taking advantage of the concurrent CB and ST measurements collected by the RpG radiometer deployed at Politecnico di Milano, Milan, Italy, under the ESA-funded WRAD project. Tests have shown that, in scattering-free conditions, the ANN prediction accuracy is comparable to the one provided by the more customary CB technique (e.g., average $\mathrm{RMS_{ANN}} = 0.18$ dB and $\mathrm{RMS_{CB}} = 0.23$ dB), while in rainy conditions, the ML approach achieves a lower estimation error (e.g., average $\mathrm{RMS_{ANN}} = 1.39$ dB and $\mathrm{RMS_{CB}} = 3.20$ dB). Based on these results, and considering the sound physical basis of the well-established CB measurement technique, an AWCPM was devised, which combines the benefits of the CB technique and of the ANN: taking advantage of the SSI to identify precipitation along the path, the former is applied in scattering free conditions, while the latter is employed during rain events. Statistical results indicate that AWCPM offers a very accurate prediction of the CCDF of A both at the Ka- and W-band, which, in turn, represents a key piece of information for the design of Earth-space links.

Starting from these encouraging but preliminary results, future work will include corroborating AWCPM by taking advantage of more extensive additional Ka-/W-band measurements collected in other sites (e.g., Rome, NY [12]): while the model's framework is expected to be applicable worldwide, the accuracy of the ANNs derived in this work for different measurement periods and in other sites might decrease. Additionally, the use of ANNs with memory layers [e.g., long short-term memory (LSTM)] will be taken into account to further improve the accuracy of AWCPM.

TABLE V
Coefficients b in (13) for Each Coefficient a in (12) at $f = 23.84$ GHz

	b_0	b_1	b_2	b_3
a_0	-53.1	-0.094	3.93	6.3×10^{-3}
a_1	0.193	-0.098	0.91	-1.65×10^{-4}
a_2	0.03	-0.089	0.138	-2.32×10^{-4}

TABLE VI
Coefficients b in (13) for Each Coefficient a in (12) at $f = 31.4$ GHz

	b_0	b_1	b_2	b_3
a_0	-26.2	-0.102	-16.2	-1.4×10^{-3}
a_1	0.098	-0.102	0.96	-7.7×10^{-5}
a_2	0.02	-0.091	0.166	-1.35×10^{-4}

TABLE VII
Coefficients b in (13) for Each Coefficient a in (12) at $f = 72.5$ GHz

	b_0	b_1	b_2	b_3
a_0	-42.4	-0.059	-16.6	-7.74×10^{-4}
a_1	0.19	-0.067	0.96	-1.08×10^{-4}
a_2	0.028	-0.026	0.165	3.32×10^{-4}

Appendix

A new analytical model is proposed to estimate the mean radiating temperature, according to its dependence on the elevation angle (as pointed out, e.g., in [8]) and on the ground values of pressure (P_S), temperature (T_S), and relative humidity (RH_S) (whose correlation with T_{mr} is discussed in [12] and [26], for example). The model was devised by resorting to ten years of radiosonde observation (RAOBS) collected twice a day (0 and 12 UTC) at Milan/Linate airport, lying at a 5 km distance from the site where the MWR is installed. As summarized in Fig. 20, the model was developed using the vertical profiles of pressure (P), temperature (T), and relative humidity (RH) as input to the MPM93 mass absorption model proposed in [33] to calculate the mean radiating temperature $T_{\mathrm{mr}}(f, \theta)$, for a given elevation angle θ and each of the four radiometric frequencies f. The analysis of the results pointed out that T_{mr} is linearly correlated to T_S and RH_S (as also discussed in [12]), and only weakly dependent on P_S, which was therefore neglected in the model development. Specifically, the following equation was used to relate the mean radiating temperature to the ground meteorological variables

$$T_{\mathrm{mr}}(f,\theta) = a_0(f,\theta) + a_1(f,\theta)T_S + a_2(f,\theta)\mathrm{RH}_S \quad (12)$$

where the coefficients $a_j(f,\theta)$ ($j = 0, 1, 2$) were regressed from the calculated $T_{\mathrm{mr}}(f,\theta)$ and the RAOBS first-level values of the temperature (T_S—in K) and relative humidity (RH_S—in %) profiles (see Fig. 20).

The process illustrated in Fig. 20 was repeated for different elevation angles, ranging from 10° to 90°. Finally, the following double exponential model for the coefficients a_0, a_1, and

TABLE VIII

COEFFICIENTS B IN (13) FOR EACH COEFFICIENT A IN (12) AT $f = 82.5$ GHz

	b_0	b_1	b_2	b_3
a_0	-63.3	-0.078	-22.07	-0.0026
a_1	0.24	-0.08	0.99	-1.84×10^{-4}
a_2	0.043	-0.057	0.167	-6.49×10^{-5}

TABLE IX

MEAN VALUE (K) OF THE ERROR FIGURE IN (14)

	10°	20°	30°	40°	50°	60°	70°	80°	90°
23.84 GHz	0.1	0.1	0.1	0.1	0.1	0.1	0.1	0.1	-0.1
31.4 GHz	1.2	1.2	1.1	1.1	1.1	1.1	1.1	1.1	1.1
72.5 GHz	1.9	1.6	1.3	1.2	1.2	1.2	1.2	1.1	1
82.5 GHz	1.4	1.2	0.9	0.9	0.9	0.9	0.9	0.9	0.8

TABLE X

ROOT MEAN SQUARE VALUE (K) OF THE ERROR FIGURE IN (14)

	10°	20°	30°	40°	50°	60°	70°	80°	90°
23.84 GHz	2.8	2.9	2.9	3	3	3	3	3	3
31.4 GHz	3.1	3.2	3.2	3.2	3.2	3.2	3.2	3.2	3.2
72.5 GHz	3.4	3.3	3.1	3.1	3.1	3.1	3.1	3.1	3
82.5 GHz	3.1	3.1	3.1	3.1	3.1	3.1	3.1	3.1	3.1

a_2 was derived

$$a_j(f,\theta) = b_{0,j}(f)e^{b_{1,j}(f)\theta} + b_{2,j}(f)e^{b_{3,j}(f)\theta} \tag{13}$$

where $j = 0, 1, 2$ indicates the a coefficient number and θ is the elevation angle expressed in degrees. The coefficients $b_{k,j}(k = 0, 1, 2, 3$ indicating the b coefficient number) are listed in Tables V–VIII for 23.84, 31.4, 72.5, and 82.5 GHz, respectively.

As an example, Fig. 21 shows the trend of coefficient a_2 at $f = 82.5$ GHz, which is precisely fit by the expression in (13). Similar results are obtained for a_0 and a_1.

Fig. 22 shows the trend of $T_{\rm mr}$ as a function of the elevation angle according to the model in (12), for $T_S = 288$ K and $\mathrm{RH}_S = 50\%$: the 10°–90° peak-to-peak variation of $T_{\rm mr}$ is approximately 2, 1.5, 7, and 4 K at 23.84, 31.4, 72.5, and 82.5 GHz, respectively.

Fig. 23 compares the mean radiating temperature as calculated from the RAOBS profiles (see Fig. 20) and as estimated using the analytical model in (12). Results refer to two full years of the available dataset at $f = 82.5$ GHz and $\theta = 45°$.

The discrepancy between the curves in Fig. 23 can be quantified by using the error figure ε defined as

$$\varepsilon(t, f, \theta) = T^E_{\rm mr}(t, f, \theta) - T^M_{\rm mr}(t, f, \theta)\ \text{(K)} \tag{14}$$

where $T^E_{\rm mr}(t, f, \theta)$ and $T^M_{\rm mr}(t, f, \theta)$ are the mean radiating temperatures estimated using the model in (12) and calculated from the RAOBS measurements, respectively, and t represents the RAOBs launch number. Tables IX and X offer a comprehensive description of the $T^M_{\rm mr}$ model performance by listing the mean value (E) and the root mean square (rms) value of the error figure in (14), for each of the four radiometric frequencies and as a function of selected elevation angles. Results indicate quite a stable performance, with E ranging between -0.1 K and 1.9 K, and with rms limited to 3.4 K.

ACKNOWLEDGMENT

The authors would like to thank NASA for making available the rain rate data within the collaboration with Politecnico di Milano, Milan, Italy, on the Alphasat Aldo Paraboni propagation experiment and Simone Sipala for his help with the calculations on the data.

REFERENCES

[1] C. Riva, C. Capsoni, L. Luini, M. Luccini, R. Nebuloni, and A. Martellucci, "The challenge of using the W band in satellite communication," *Int. J. Satellite Commun. Netw.*, vol. 32, no. 3, pp. 187–200, 2014.

[2] J. E. Allnutt, *Satellite to Ground Radiowave Propagation*, 2nd ed. London, U.K.: Institution of Engineering and Technology, Mar. 2011.

[3] F. Cuervo, A. M. Polegre, D. Vanhoenacker-Janvier, J. Flávio, and M. Schmidt, "The Q/W-band CubeSat LEO propagation experiment," in *Proc. 15th Eur. Conf. Antennas Propag. (EuCAP)*, Dusseldorf, Germany, Mar. 2021, pp. 1–5.

[4] *Propagation Data and Prediction Methods Required for the Design of Earth-Space Telecommunication Systems*, document Recommendation ITU-R P.618-13, Geneva, Switzerland, 2017.

[5] G. Codispoti et al., "The role of the Italian space agency in investigating high frequencies for satellite communications: The alphasat experiment," *Int. J. Satell. Commun. Netw.*, vol. 37, no. 5, pp. 387–396, Sep. 2019.

[6] F. Giannetti, M. Moretti, R. Reggiannini, and A. Vaccaro, "The NEFOCAST system for detection and estimation of rainfall fields by the opportunistic use of broadcast satellite signals," *IEEE Aerosp. Electron. Syst. Mag.*, vol. 34, no. 6, pp. 16–27, Jun. 2019.

[7] L. Luini, C. Riva, C. Capsoni, and A. Martellucci, "Attenuation in nonrainy conditions at millimeter wavelengths: Assessment of a procedure," *IEEE Trans. Geosci. Remote Sens.*, vol. 45, no. 7, pp. 2150–2157, Jul. 2007.

[8] Y. Han and E. R. Westwater, "Analysis and improvement of tipping calibration for ground-based microwave radiometers," *IEEE Trans. Geosci. Remote Sens.*, vol. 38, no. 3, pp. 1260–1276, May 2000.

[9] L. Luini, C. Riva, R. Nebuloni, M. Mauri, J. Nessel, and A. Fanti, "Calibration and use of microwave radiometers in multiple-site EM wave propagation experiments," in *Proc. EuCAP*, Aug. 2018, pp. 1–5.

[10] L. Tsang, J. Kong, E. Njoku, D. Staelin, and J. Waters, "Theory for microwave thermal emission from a layer of cloud or rain," *IEEE Trans. Antennas Propag.*, vol. AP-25, no. 5, pp. 650–657, Sep. 1977.

[11] D. Long and F. Ulaby, *Microwave Radar and Radiometric Remote Sensing*. Norwood, MA, USA: Artech House, 2015.

[12] F. S. Marzano, V. Mattioli, L. Milani, K. M. Magde, and G. A. Brost, "Sun-tracking microwave radiometry: All-weather estimation of atmospheric path attenuation at *Ka*-, *V*-, and *W*-band," *IEEE Trans. Antennas Propag.*, vol. 64, no. 11, pp. 4815–4827, Nov. 2016.

[13] V. Mattioli, L. Milani, K. M. Magde, G. A. Brost, and F. S. Marzano, "Retrieval of sun brightness temperature and precipitating cloud extinction using ground-based sun-tracking microwave radiometry," *IEEE J. Sel. Topics Appl. Earth Observ. Remote Sens.*, vol. 10, no. 7, pp. 3134–3147, Jul. 2017.

[14] L. Luini et al., "Development and application of advanced experimental techniques for ground microwave radiometry in all weather conditions," in *Proc. 17th Eur. Conf. Antennas Propag. (EuCAP)*, Florence, Italy, Mar. 2023, pp. 1–5.

[15] F. J. Tapiador, C. Kidd, K.-L. Hsu, and F. Marzano, *Neural Networks in Satellite Rainfall Estimation*. London, U.K.: Royal Meteorological Society (RMetS), 2006.

[16] F. Tapiador et al., "A neural networks-based fusion technique to estimate half-hourly rainfall estimates at 0.1° resolution from satellite passive microwave and infrared data," *J. Appl. Meteorol.*, vol. 43, no. 4, pp. 576–594, 2004.

[17] G. Rivolta, F. S. Marzano, E. Coppola, and M. Verdecchia, "Artificial neural-network technique for precipitation nowcasting from satellite imagery," *Adv. Geosci.*, vol. 7, pp. 97–103, Feb. 2006.

[18] F. S. Marzano, E. Fionda, and P. Ciotti, "Neural-network approach to ground-based passive microwave estimation of precipitation intensity and extinction," *J. Hydrol.*, vol. 328, nos. 1–2, pp. 121–131, Aug. 2006.

[19] L. Wu et al., "Prediction of atmospheric noise temperature at the deep space network with machine learning," *Radio Sci.*, vol. 57, no. 11, pp. 1–11, Nov. 2022.

[20] M. Biscarini et al., "Statistical modeling of atmospheric propagation channel at W-band through sun-tracking microwave radiometric measurements for non-geostationary satellite links," *IEEE Trans. Antennas Propag.*, vol. 71, no. 9, pp. 7512–7522, Sep. 2023.
[21] F. T. Ulaby, R. K. Moore, and A. K. Fung, *Microwave Remote Sensing*. Reading, MA, USA: Addison-Wesley, 1981.
[22] R. M. Allnutt, "Use of radiometers in atmospheric attenuation measurements," *IEE Proc. Microw., Antennas Propag.*, vol. 141, no. 5, p. 428, 1994.
[23] M. Biscarini and F. S. Marzano, "Generalized parametric prediction model of the mean radiative temperature for microwave slant paths in all-weather condition," *IEEE Trans. Antennas Propag.*, vol. 68, no. 2, pp. 1031–1043, Feb. 2020.
[24] S. I. Karhu, P. Jokela, and E. T. Salonen, "Atmospheric attenuation statistics of 11 years measured by a 12 GHz radiometer in Finland," in *Proc. 21st Eur. Microw. Conf.*, Stuttgart, Germany, Oct. 1991, pp. 1229–1234.
[25] R. R. Bell, "Calibration of 20 and 30 GHz radiometers by using the ATS-6 satellite beacons," *Electron. Lett.*, vol. 13, pp. 412–413, Jan. 1977.
[26] G. Brost and K. Magde, "On the use of the radiometer formula for atmospheric attenuation measurements at GHz frequencies," in *Proc. 10th Eur. Conf. Antennas Propag. (EuCAP)*, Apr. 2016, pp. 1–5.
[27] G. K. Baydoğmuş, "The effects of normalization and standardization an Internet of Things attack detection," *Eur. J. Sci. Technol.*, no. 29, pp. 187–192, Dec. 2021.
[28] N. M. Nawi, W. H. Atomi, and M. Z. Rehman, "The effect of data preprocessing on optimized training of artificial neural networks," in *Proc. 4th Int. Conf. Electr. Eng. Informat. (ICEEI)*, Jan. 2013, pp. 1–8.
[29] T. Zhan, M. Gong, X. Jiang, and S. Li, "Log-based transformation feature learning for change detection in heterogeneous images," *IEEE Geosci. Remote Sens. Lett.*, vol. 15, no. 9, pp. 1352–1356, Sep. 2018.
[30] E. Alpaydin, *Introduction to Machine Learning*, 4th ed. Cambridge, MA, USA: MIT Press, 2020.
[31] (2021). *MathWorks. Fitrnet-Train Neural Network Regression Model*. [Online]. Available: https: //ch.mathworks.com/help/stats/fitrnet.html
[32] A. V. Bosisio, E. Fionda, P. Ciotti, and A. Martellucci, "A sky status indicator to detect rain-affected atmospheric thermal emissions observed at ground," *IEEE Trans. Geosci. Remote Sens.*, vol. 51, no. 9, pp. 4643–4649, Sep. 2013.
[33] H. J. Liebe, G. A. Hufford, and M. G. Cotton, "Propagation modelling of moist air and suspended water/ice particles at frequencies below 1000 GHz," in *Proc. AGARD 52nd Spec. Meeting EM Wave Propag.*, Nov. 1993, pp. 1–4.

Tuna Tunçkol was born in Istanbul, Turkey, in 1994. He received the bachelor's degree in mechanical engineering from Koç University, Istanbul, and the master's degree in space engineering from Politecnico di Milano, Milan, Italy.

He is currently working as a Satellite Research and Development Engineer at Fergani Space Technologies, Istanbul, Turkey. His focus is mainly on mechanical design, structural analysis, and structural subsystem verification of the satellite. Furthermore, he has experience in neural networks and their applications in satellite communications, and finite element analysis. Now, his research includes integrating machine learning with his fundamental knowledge of space systems, particularly in structural and telecommunication subsystems.

Marianna Biscarini (Senior Member, IEEE) received the M.Sc. degree (cum laude) in electronic engineering and the Ph.D. degree in electromagnetism from the Sapienza University of Rome, Rome, Italy, in 2012 and 2016, respectively.

Since 2012, she has been with the Department of Information Engineering, Electronics and Telecommunications (DIET), Sapienza University of Rome, and CETEMPS, University of L'Aquila, L'Aquila, Italy, working on electromagnetic wave propagation through the atmosphere: physical modeling for electromagnetic propagation applications, such as attenuation due to rain/ice particles, scintillation effects, and expected impact on SatCom links, remote sensing of atmospheric constituents using radiometric data, dimensioning of SatCom systems (deep-space, GEO, MEO, and LEO), also exploiting weather forecast models and Propagation Impairment Mitigation Techniques (PIMT), such as site/smartgateway/frequency diversity and adaptive code modulation. She is currently an Assistant Professor with DIET involved in several international projects, most of them commissioned to the research group by the European Space Agency (ESA), the USA Air Force Laboratory (AFRL), and Thales Alenia Space Italy.

Lorenzo Luini (Senior Member, IEEE) received the Laurea degree (cum laude) in telecommunication engineering and the Ph.D. degree (cum laude) in information technology from Politecnico di Milano, Milan, Italy, in 2004 and 2009, respectively.

He is currently an Associate Professor at the Dipartimento di Elettronica, Informazione e Bioingegneria (DEIB), Politecnico di Milano. He has been involved in several European COST projects, in the European Satellite Network of Excellence (SatNEx), as well as in several projects commissioned to the research group by the European Space Agency (ESA), the USA Air Force Laboratory (AFRL), and the European Commission (H2020). He has authored 240 contributions to international conferences and scientific journals. His research activities are focused on electromagnetic wave propagation through the atmosphere, both at radio and optical frequencies.

Dr. Luini is a member of the Italian Society of Electromagnetism, the Chair of the Working Group "Propagation" of European Association on Antennas and Propagation (EurAAP), and the Leader of the Working Group "Propagation Data Calibration" within the AlphaSat Aldo Paraboni Propagation Experimenters (ASAPE) Group. He is an Associate Editor of IEEE TRANSACTIONS ON ANTENNAS AND PROPAGATION (TAP) and *International Journal on Antennas and Propagation* (IJAP).

Open Access funding provided by 'Politecnico di Milano' within the CRUI CARE Agreement